



Mechanical behavior and microstructure of $Ti_{20}Hf_{20}Zr_{20}Ta_{20}Nb_{20}$ high-entropy alloy loaded under quasi-static and dynamic compression conditions



G. Dirras ^{a,*}, H. Couque ^b, L. Lilensten ^c, A. Heczel ^d, D. Tingaud ^a, J.-P. Couzinié ^c, L. Perrière ^c, J. Gubicza ^d, I. Guillot ^c

^a Université Paris 13, Sorbonne Paris Cité, LSPM-CNRS, UPR 3407, 99 avenue JB Clément, 93430 Villetaneuse, France

^b Nexter-munitions, 7 Route de Guerry, 18200 Bourges, France

^c Université Paris Est, ICMPE (UMR 7182), CNRS, UPEC, 94320 Thiais, France

^d Department of Materials Physics, Eötvös Loránd University, Budapest, P.O.B. 32, H-1518, Hungary

ARTICLE INFO

Article history:

Received 20 August 2015

Received in revised form 19 October 2015

Accepted 22 November 2015

Available online 23 November 2015

Keywords:

High-entropy alloy

Impact loading

Mechanical behavior

Electron backscatter diffraction

Shear bands

ABSTRACT

The microstructure and the mechanical behavior of equimolar $Ti_{20}Hf_{20}Zr_{20}Ta_{20}Nb_{20}$ high-entropy alloy in a wide range of initial strain rates between $\sim 10^{-3} \text{ s}^{-1}$ and $\sim 3.4 \times 10^3 \text{ s}^{-1}$ were studied. A significant increment in the yield strength with increasing strain rate was observed. The yield strength at $\sim 3.4 \times 10^3 \text{ s}^{-1}$ was about 40% higher than that measured at $\sim 10^{-3} \text{ s}^{-1}$. Analysis by electron backscatter diffraction shows that in the low strain rate regime (up to $\sim 10 \text{ s}^{-1}$) the deformation occurs mainly in evenly distributed bands, while in the dynamic regime the deformation is strongly localized in macroscopic shear bands accompanied by softening even after the onset of yielding. The Kernel Average Misorientation technique reveals a high level of lattice rotation within these bands that also carries intense shear. In addition, X-ray diffraction line profile analysis indicates that the sharp increase in the flow stress is mostly related to an increase of the dislocation density.

© 2015 Elsevier Inc. All rights reserved.

1. Introduction

Since the pioneering work by Cantor et al. [1] and Yeh et al. [2], high-entropy alloys (HEAs) have triggered a lot of enthusiasm in materials science community and became a hot topic as indicated by the detailed reviews about this alloy family [3,4]. From the available literature data, two main families of HEAs have been investigated so far: face-centered cubic (fcc) CoCrCuFeNi-based alloys which transform to body-centered cubic (bcc) structures with addition of Al, Ti, and Mn [5–11], and refractory bcc simple solid solution counterparts initiated by Senkov et al. [12–18] and others [19–25]. Indeed, HEAs have drawn more and more attention due to their outstanding mechanical characteristics besides other attractive properties such as large saturation magnetization [26], high thermal stability and good oxidation resistance. For instance, Gali and George [27] studied the mechanical behavior of CrMnFeCoNi and CrFeCoNi alloys and they found that the strength depends strongly on the temperature between 77 and 1273 K, while a relatively weak strain-rate dependence of the strength was observed in the range of 10^{-3} – 10^{-1} s^{-1} . It was also shown that the ductility did not vary inversely with the yield strength. A strong work hardening was observed that was attributed to deformation-induced

nanotwinning. Zhu and coworkers [28] studied the nature of incipient plasticity in FeCoCrMnNi HEA by instrumented nanoindentation. The maximum shear stress required to initiate plasticity was found to be within 1/15 to 1/10 of the shear modulus and relatively insensitive to grain orientation. Quasi-static compression tests were performed on an equiatomic CoCrFeMnNi high-entropy alloy in a temperature range between 77 and 1073 K [29]. The underlying deformation mechanisms were determined. These include planar dislocation glide in the normal fcc slip systems in the initial stage of plasticity and enhanced ductility observed at 77 K that was attributed to a dynamical Hall–Petch effect due to deformation twinning. Wu and coworkers have shown that the plastic deformation in multi-component fcc HEAs was caused by the motion of mixed dislocations similar to the conventional fcc metals [30]. It was also found that for annealed FeCoNiCrMn HEAs the hardness versus grain size relationship follows the classical Hall–Petch strengthening, though with a relatively high hardening coefficient [31]. Patriarca and coworkers [32] conducted experimental and theoretical investigations on the plastic behavior of single crystalline FeNiCoCrMn HEA. The critical resolved shear stress obtained experimentally (175 MPa) was in good agreement with the value determined by atomistic-modified Peierls–Nabarro model calculations (178 MPa). At the same time, an abnormally strong temperature dependence of the critical resolved shear stress was reported below 293 K as compared to conventional fcc metals [33]. Stepanov and coworkers [34] have studied the

* Corresponding author.

E-mail address: dirras@univ-paris13.fr (G. Dirras).

microstructure evolution in CoCrFeNiMn HEA during uniaxial compression in the temperature range of 873–1373 K. Discontinuous dynamic recrystallization was found to be active during both warm (below 1073 K) and hot (above 1073 K) deformations. The creep deformation was studied at 880 and 1000 K and a strain rate of $6.7 \times 10^{-6} \text{ s}^{-1}$ using in-situ neutron diffraction [35]. It was shown that the dominant deformation mode is the dislocation glide at 800 K and diffusion-controlled dislocation creep at 1000 K. Exceptional damage tolerance with tensile strengths above 1 GPa and fracture toughness values exceeding $200 \text{ MPa} \cdot \text{m}^{1/2}$ in CrMnFeCoNi high-entropy alloy were also reported [36]. Sluggish diffusion kinetics has been often observed as an important effect that contributes to the outstanding properties of HEAs. The diffusion couple method was used to measure the diffusion parameters of Co, Cr, Fe, Mn and Ni in ideal-solution-like Co–Cr–Fe–Mn–Ni alloys [37]. It was shown that the diffusion coefficients in the Co–Cr–Fe–Mn–Ni alloys are indeed lower than those in the reference metals. In addition, the corresponding higher diffusion activation energies of the investigated HEAs accounted for sluggish diffusion in these alloys.

Apart from a recent paper dealing with the dynamic behavior of HEAs by Kumar and co-authors [38] in the vast majority of studies on HEAs, the mechanical properties have been mainly investigated via hardness and compression tests while only a few works have been devoted to the tensile behavior of HEAs [39,40].

However, the application of this new kind of promising materials requires the study of its mechanical performance and microstructure evolution in practical deformation processes such as rolling, machining and impact loading. In these processes the strain rate is in the range between 1 and 10^4 s^{-1} . In this strain rate range, flow stress versus strain rate plot usually displays two regimes according to the active deformation mechanisms: the thermally activated regime at low strain rates and the viscous drag regime at high strain rates. The transition between the two mechanisms was found to occur at the strain rate of about 10^3 s^{-1} [41,42]. From microstructural point of view, adiabatic effects characterize the dynamic regime: dynamic recrystallization and formation of adiabatic shear bands have been reported [43–46]. However, in some cases mechanical twinning was also observed [47].

In this paper we study the mechanical behavior and the microstructure evolution in equimolar TiHfZrTaNb refractory high-entropy alloy during quasi-static and dynamic compressions. Special emphasis will be placed on the latter loading method.

2. Experimental procedures

2.1. Sample processing

The alloy of composition $\text{Ti}_{20}\text{Zr}_{20}\text{Hf}_{20}\text{Nb}_{20}\text{Ta}_{20}$ was obtained according to the following process: master alloys Ti–Zr–Hf and Nb–Ta from the high purity elements (purity exceeding 99.9%) were first arc-melted on a water-cooled copper plate under argon atmosphere. A titanium getter was melted before each alloy fusion in order to capture the residual oxygen in the chamber. Each master alloy was melted twice in order to ensure good homogeneity, and then they were mixed together. Homogeneity in the alloy was obtained by high frequency induction melting in a sectorized cooled copper crucible under helium atmosphere. Finally, the alloy was casted by arc melting. Ingots of about 60 mm in length and 10 mm in diameter were obtained.

2.2. Mechanical testing

Uniaxial compression data at strain rates ranging from $\sim 10^{-3}$ to $\sim 3.4 \times 10^3 \text{ s}^{-1}$ were obtained at room temperature on specimens 6 mm in diameter and 3.2 mm in height. A conventional testing machine was used up to the strain rate of $\sim 10 \text{ s}^{-1}$, while a Direct Impact Hopkinson Pressure Bar (DIHPB) setup was used to generate plastic deformation at higher strain rates up to $\sim 3.4 \times 10^3 \text{ s}^{-1}$ (initial strain rate

[42]). In the conventional compression tests the following strain rates were applied: 10^{-3} , 10^{-1} , 4.53 and 9.3 s^{-1} . In the DIHPB technique, originally introduced by Dharan [48], a specimen placed against a Hopkinson pressure bar is impacted by a striker moving at a constant velocity. The striker speed, V_i , typically between 5 and 100 m s^{-1} , is recorded using two laser beams separated by 18 mm and positioned 30 mm prior impact. Both striker and Hopkinson bar are made of tungsten alloy with 20 mm in diameter, 17.5 g cm^{-3} in density and 1500 MPa in yield strength. In the present study impact velocities of 3.7, 6.14 and 10.34 m s^{-1} were applied in the investigation of the macroscopic response in the dynamic regime.

2.3. Electron backscatter diffraction

Samples for electron backscatter diffraction (EBSD) investigations were prepared by mechanical grinding using 1200 to 4000 grit SiC papers followed by a final polishing step using a 20 nm alumina oxide particle suspension (OPS) from Struers™. EBSD investigations were carried out using a Zeiss Supra 40VP FEG scanning electron microscope (SEM). Due to the wide grain size distribution in the as-cast material, a step size between the neighboring measurement positions of $1 \mu\text{m}$ was used. For statistical purpose, all the scans were performed on an area greater than $1 \text{ mm} \times 1 \text{ mm}$. The data were further processed by OIM™ software version 5 from TexSem Laboratories (TSL). The “grain dilation” procedure with a single iteration step was applied to clean up misindexed points. The average grain size, the fractions of low angle grain boundaries (LAGBs) and high angle grain boundaries (HAGBs), the image quality (IQ), the grain boundary (GB) and the inverse pole figure (IPF) maps were further extracted from the EBSD scans. In addition, the Kernel Average Misorientation (KAM) function was used to determine local values of intragranular lattice rotation [49]. KAM is numerically defined as the average of misorientation between the pixel of interest and all specified nearest neighbor pixels. For a given point, the average misorientation with all neighbors is calculated with the provision that misorientations exceeding some tolerance value are excluded from averaging. For the present calculation, the 5th nearest neighbor pixels and a maximum misorientation angle of 5° (upper limit for KAM computation) were chosen, giving the largest lattice distortion of $1\%/\mu\text{m}$ at the applied kernel diameter of $10 \mu\text{m}$.

2.4. X-ray diffraction

The average lattice parameter for the deformed HEA samples was investigated by X-ray diffraction (XRD) using a Philips Xpert Θ – 2Θ powder diffractometer operating at 40 kV and 30 mA with $\text{CuK}\alpha$ radiation (wavelength: $\lambda = 0.15418 \text{ nm}$). The scan rate was $1.4 \times 10^{-3} \text{ degree/s}$. According to the measured XRD patterns all the studied samples have bcc structure. The average lattice parameter was determined from the diffraction peak positions using the Nelson–Riley method [50].

The lattice defect structure in the samples was studied by X-ray line profile analysis (XLPA). The X-ray line profiles were measured by a high-resolution rotating anode diffractometer (type: RA-MultiMax9, manufacturer: Rigaku) operating at 40 kV and 100 mA with $\text{CuK}\alpha_1$ (wavelength, $\lambda = 0.15406 \text{ nm}$) radiation. The diffraction profiles were evaluated by the Convolutional Multiple Whole Profile (CMWP) method [51]. In this procedure, the diffraction pattern is fitted by the sum of a background spline and the convolution of the instrumental pattern and the theoretical line profiles related to crystallite size and dislocations. The instrumental pattern was measured on a LaB_6 standard sample (SRM 660). The area-weighted mean crystallite size ($\langle x \rangle_{\text{area}}$) and the dislocation density (ρ) were determined by the CMWP method. This evaluation procedure requires the knowledge of the elastic anisotropy factor of the studied HEA crystal which is not available in the literature. Therefore, the elastic anisotropy factor A of the present HEA material was estimated from the elastic response of grains with different orientations on nanoindentation. The detail of this procedure is

given elsewhere [52] which yields 2.3 ± 0.2 for A . With this anisotropy factor, the dislocation contrast factors influencing peak broadening was determined and used in the present CMWP evaluation [52].

3. Results and discussion

3.1. Mechanical behavior

Fig. 1a and b show typical true stress versus true plastic strain plots for strain rates in the quasi-static (**Fig. 1a**) and in the dynamic (**Fig. 1b**) regimes, respectively. It is noted that in the case of the DIHPB tests, the strain extracted from strain gauge measurements was limited to a plastic strain of 0.3 as beyond the strain of about 0.45, the conditions for a uniaxial deformation state are no longer strictly fulfilled. While a continuous strain hardening is observed for the samples strained in the low strain rate regime (**Fig. 1a**), a softening behavior just after the onset of yielding is revealed for the samples deformed in the high strain rate regime (**Fig. 1b**). This behavior is related to deformation localization in (multiple) shear/adiabatic shear bands (see the microstructure investigation section).

Fig. 2 shows the flow stresses at 0.002 and 0.05 offset strains (hereafter referred to as yield strength and flow stress, respectively) as a function of the logarithm of the strain rate applied in compression loading. During DIHPB tests the strain rate continuously increases with increasing strain. At the strain of 0.002 the impact velocities of 3.7, 6.14 and 10.34 m s^{-1} correspond to the strain rates of 1400, 2100 and 3450 s^{-1} , respectively, and these values are used in **Fig. 2**. Similar to other materials both the yield strength and the flow stress increase with increasing strain rate. This increment becomes faster for the strain rates between $\sim 10^3$ and $\sim 10^4 \text{ s}^{-1}$, as indicated by the change in the slope of the red straight lines in **Fig. 2** (they are only guide for eyes). Former results obtained on other materials suggest that this behavior is most probably related to a transition in the deformation processes from thermally activated overcoming of obstacles by dislocations in the quasi-static regime to viscous drag-controlled dislocation motion in the dynamic regime [53]. It should be noted that the increase in the stress at high strain rates might also be caused by the increase in the dislocation density [54,55]. **Fig. 2** also shows that with increasing strain rate the gap between the yield strength (measured at 0.002 offset

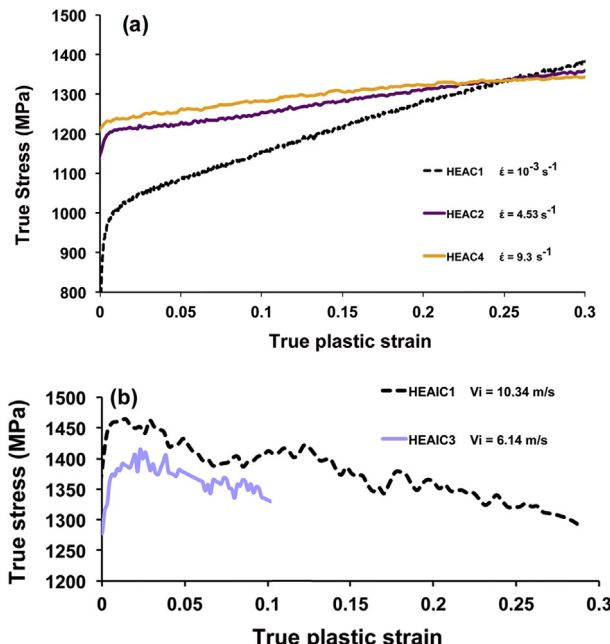


Fig. 1. Typical true stress versus true plastic strain plots for strain rates in the quasi-static (a) and in the dynamic (b) regimes.

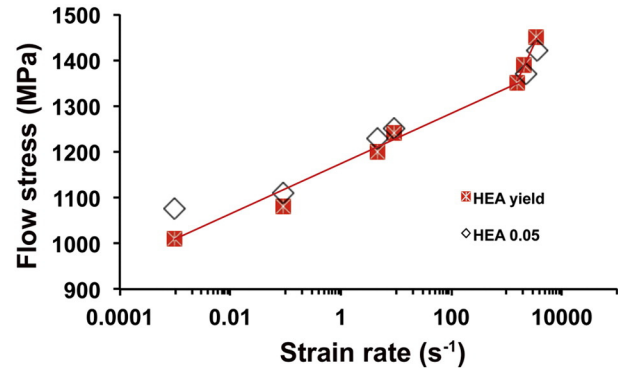


Fig. 2. The yield strength and the flow stress at 0.05 offset strain as a function of the logarithm of the strain rate applied in compression loading. The red line is a guide for the eye, indicating the trend in the yield strength.

strain) and the flow stress determined at the strain of 0.05 progressively reduces and ultimately the flow stress at 0.05 offset became lower than the yield stress. This behavior indicates an early softening after yielding occurred at high strain rates.

In the case of the impacted samples, the flow stress measured in-situ at the end of the impact test can be compared with the flow stress determined ex-situ after deformation as one third of the hardness. The hardness values were obtained by a Zwick Roell ZH μ Vickers indenter using an applied load of 10 N and a dwell time of 10 s. For the specimen deformed at a velocity of 10.34 m s^{-1} the hardness was determined after the impact test which state corresponds to a plastic strain of 0.49 and a strain rate of $\sim 4700 \text{ s}^{-1}$. The flow stress calculated from the hardness was 1228 MPa which is in a reasonable agreement with the flow stress value obtained in-situ at the end of impact deformation (not shown in **Fig. 1b**). This observation suggests that the strain rate effect on the mechanical behavior could be explained with the help of post-mortem microstructure investigations presented below.

3.2. Microstructure investigation by EBSD

3.2.1. The as-cast microstructure

Fig. 3a and b show IPF and IQ + GB maps for the as-cast microstructure, respectively. The material exhibits a random crystallographic texture and the grain size values are in the range of $10\text{--}350 \mu\text{m}$ with an average value of $\sim 200 \mu\text{m}$. As it was revealed in a previous study [22], the size and morphology of grains as well as the chemical composition depend on the cooling rate during HEA processing. Indeed, it was shown that in the upper part of the ingot (lower cooling rate) the grains have a dendritic structure (see **Fig. 3** in ref. [22]) and the dendrite arms are mostly composed of Ta and Nb while micro-segregations consisting of Ti, Zr and Hf rich zones are found in the interdendritic zones.

3.2.2. The microstructure after plastic deformation at different strain rates

As an example for the microstructure developed in the low strain rate regime, **Fig. 4** shows EBSD images obtained on the sample deformed up to a true strain of ~ 0.87 at a strain rate of $\sim 4.53 \text{ s}^{-1}$. These observations were carried out in a transverse plane containing the compression direction which is vertical in the figure. The combined IPF + IQ map in **Fig. 4a** indicates an intense slip activity: individual grains are subdivided into elongated strips due to plastic deformation in slip planes. The slip traces are more or less curved due to lattice rotation accompanying the plastic deformation. In addition, slip traces appear mostly in bundles (slip bands) and they seem to interact with grain boundaries or other slip traces, giving rise to wavy-like features as seen in many locations in the map (exemplified by red lines in the KAM map, **Fig. 4b**). Such wavy effects have been recently observed by Guo et al. [56] in as-cast MoNbHfZrTi refractory HEA that was deformed at elevated temperatures. **Fig. 4a** also shows color gradient inside the

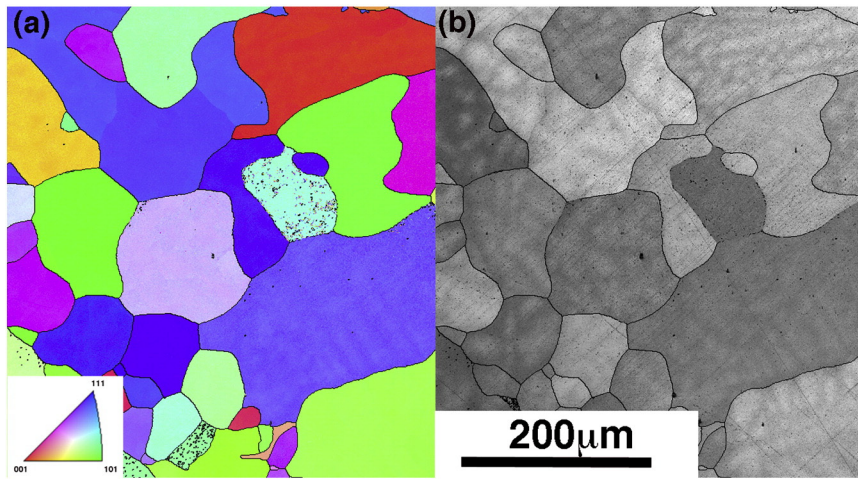


Fig. 3. A typical as-cast microstructure obtained by EBSD: (a) IPF map and (b) IQ + GB map.

grains which indicates changes in crystallographic orientation due to plastic deformation, mainly in the vicinity of grain boundaries.

The KAM map shown in Fig. 4b illustrates the lattice rotations which occur most probably due to dislocations stored in the lattice. Actually, when dislocations form in materials, their elastic strain field yields local variation in lattice orientation. In line with the discussion above, a high level of lattice rotation due to dislocation storage occurs within the slip trace bundles (red color) and in the vicinity of grain boundaries (indicated by red and yellow colors). At the same time, the strips delineated by slip plane traces display lower KAM values meaning low dislocation storage as compared to the slip bundles. Thus, from the macroscopic point of view, the slip traces appear to be well distributed, but at the grain level the dislocation activity is strongly heterogeneous.

The EBSD images in Fig. 5a–c show the microstructure after impact at a velocity of 10.34 m s^{-1} . The true strain and the strain rate in this state are about 0.49 and 4700 s^{-1} , respectively. The IPF map in Fig. 5a shows stronger deformation heterogeneity during impact test as compared to low strain rate deformation (see Fig. 4). A macroscopic band can be seen which crosses many grains and subdivides the image into two parts. The upper left part appears to be less deformed, except some areas with color gradient that indicates lattice rotations occurring there. The right bottom part is clearly much more deformed. In addition to frequent color change, lamellar/lenticular-like needles can be seen (see for example grains marked by A, B and C in Fig. 5a), growing from grain boundaries. Actually such features have also been reported in previous studies [15,36,38]. In the pioneering work by Senkov et al. [15] such features were identified as a mixture of distorted shear bands and twins. The authors estimated the threshold stress for twinning somewhere above 600 MPa in TiHfZrTaNb equimolar HEA, which was deformed by compression at room temperature in the quasi-static regime. Meyers et al. [57] reported that in polycrystalline tantalum shock-deformed at strain rates between 10^4 and 10^6 s^{-1} , twinning is expected when the flow stress is in the range of ~ 750 – 950 MPa. In the present case, although the highest achieved strain rate is lower, the flow stress reaches ~ 1500 MPa, which could be certainly enough to trigger twinning. Nevertheless, it was observed that these features also occur even if the sample is deformed in the lower strain rate regime since the flow stress can reach the critical stress value necessary for twinning due to the hardening of the sample. Therefore we think that there is no direct link between the occurrence of twinning and the strain rate per se.

As shown by IQ + GB map in Fig. 5b, the microstructure within the band could not be resolved in the present EBSD experiments, probably due to the strong lattice distortion. The blue and green lines in Fig. 5b are LAGBs with misorientation angles between 2 and 5° and 5 – 15° , respectively. Their inhomogeneous distribution at the two sides of the shear band illustrates well the deformation heterogeneity. In order to complete the IQ + GB map of Fig. 5b KAM investigation was also performed which is illustrated in Fig. 5c. Actually, unlike IQ parameter, KAM value depends mainly on the EBSD grid pitch and SEM resolution, while it is pretty immune to external factors such as surface relief [58]. The KAM map clearly shows that the elastic strain mainly localizes within the band. As discussed by Dodd and Bay [59], localization of plastic deformation usually stems from localized heating. This flow localization is often catastrophic leading to fracture by intense localized shearing. This localized shearing was called adiabatic shearing by Zener and Hollomon [60]. Such localized shear in a shear/adiabatic shear band (SB/ASB) is illustrated in Fig. 6 for the sample impacted up to a true strain of ~ 0.49 at a velocity of 10.34 m s^{-1} (corresponds to a

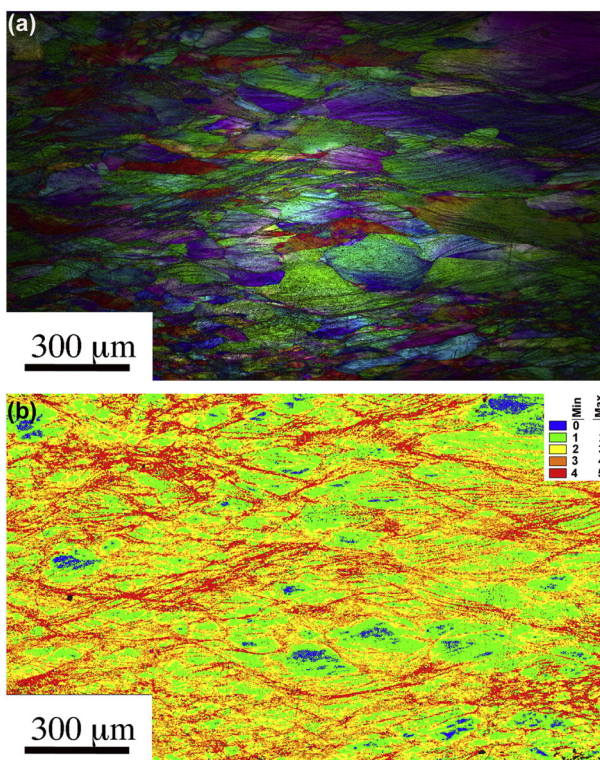


Fig. 4. EBSD images obtained on the sample deformed up to a true strain of ~ 0.87 at the strain rate of $\sim 4.53 \text{ s}^{-1}$. A combined IPF + IQ map (a) and KAM map (b). See the text for more details.

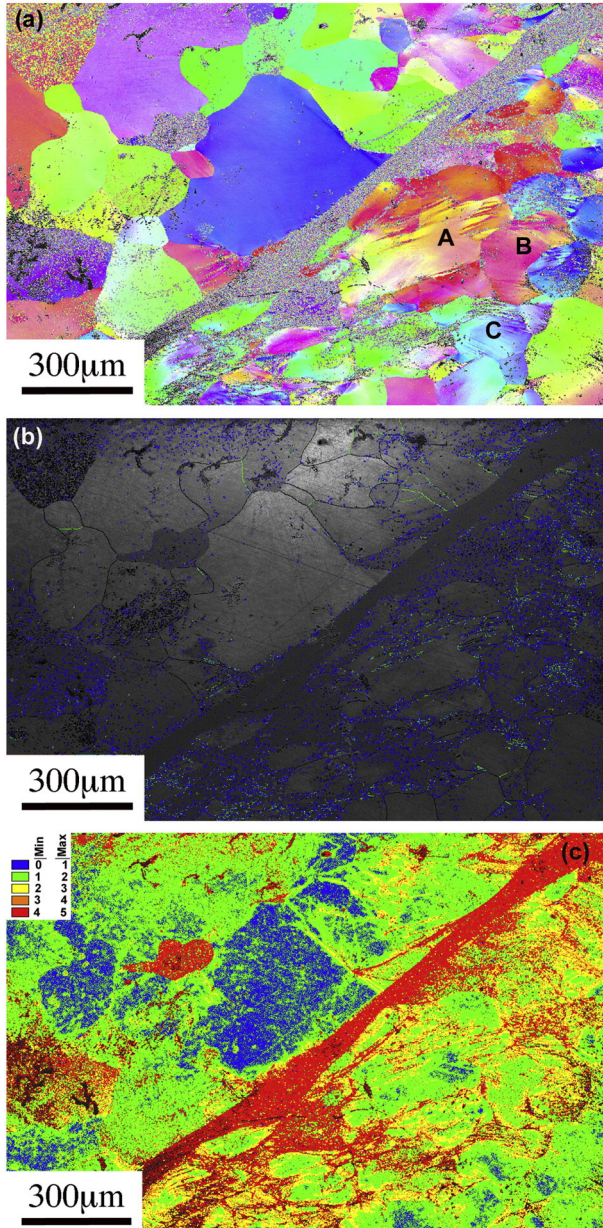


Fig. 5. EBSD images showing the microstructure after impact deformation up to a true strain of ~ 0.49 at a velocity of 10.34 m s^{-1} (corresponds to a strain rate of 4700 s^{-1}). IPF map (a); IQ + GB map (b) and KAM map (c). See the text for more details.

strain rate of 4700 s^{-1}). Indeed, shear offsets can be seen where it interacts with the needle-like features in the area marked by A in Fig. 6a. This observation also indicates that the shear banding occurs later than the formation of needles during deformation. Other features such as very thin SBs within the grains (in the area marked by B and also the features indicated by black arrows), and more thicker “lamellar” structures (indicated by white arrows) are also seen. In a previous study, similar lamellar features have been identified as mixtures of twins and SBs [15]. Similar structures have been recently reported in α -Ti and identified as kink bands [61]. Fig. 6b is an enlarged GB map of the area marked by A in Fig. 6a. The shearing of the lamellar/lenticular band is clearly visible. The white arrow represents a line scan along which the point-to-point misorientation angles have been calculated (see the inset in the upper right corner of Fig. 6b). Examination of the computed misorientation along the scan line shows that the misorientations across the scanned boundaries are lower than that expected for perfect $\Sigma 3$ twin boundaries-TBs (60° around $<111>$, which is the normal of the

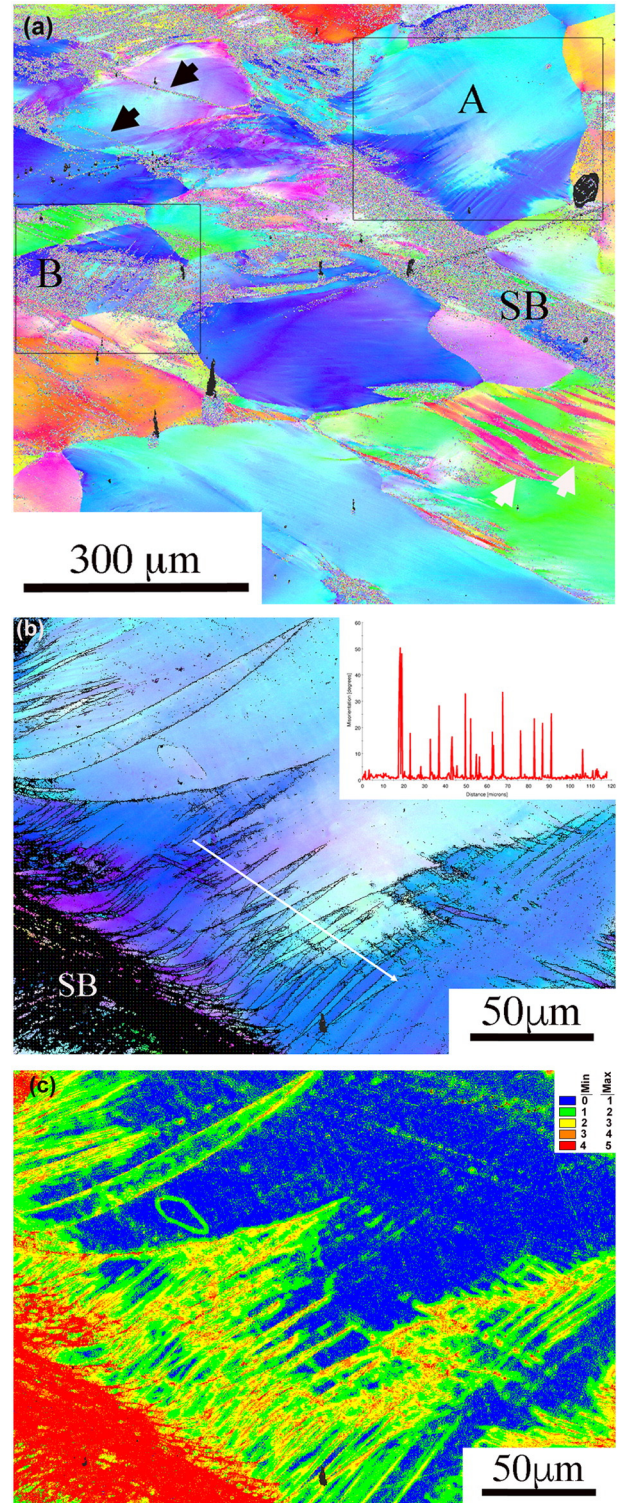


Fig. 6. (a) IPF map illustrating the localized deformation around a shear band (SB) in the sample impacted up to a true strain of ~ 0.49 at a velocity of 10.34 m s^{-1} (corresponds to a strain rate of 4700 s^{-1}). Shear offsets can be seen where SB interacts with the needle-like features in the area marked by A. Very thin SBs within the grains (in the area marked by B and also the features indicated by black arrows), and more thicker “lamellar” structures (indicated by white arrows) can also be observed. (b) is an enlarged GB map of the area marked by A in (a). The inset in (b) shows a point-to-point misorientation angle distribution along the white arrow. (c) is a KAM map of (b) illustrating the large lattice distortion within the SB and in the vicinity of the boundaries of the lenticular structures.

investigated grain). Therefore, these boundaries could not be considered as TBs. Additional work is needed to clarify this point. Finally, KAM map shown in Fig. 6c illustrates well the large lattice distortion within the SB and in the vicinity of the boundaries of the lenticular structures.

It has been shown in former works that during plastic deformation of metallic materials grain refinement occurs in adiabatic shear bands, as a consequence of dynamic recrystallization (DRX) [62–64]. DRX is a structural rearrangement whereby the initial grain structure of a material gets refined due to the formation and growth of new nanograins [65]. Nevertheless, in the case of Ta and Ta-W alloys it was reported [66] that grain refinement by DRX is a sluggish process that cannot take place in a short period of time such as the duration of the present impact test ($\sim 10^{-4}$ s). Therefore, the probability of the occurrence of recrystallization phenomenon in our experiments is very remote, which could be related to the sluggish diffusion in HEAs [1]. Indeed, the present KAM investigation also showed that the lattice distortion due to dislocation storage is high in the shear bands which observation may also exclude any DRX process as a process responsible for the observed macroscopic softening. In addition, it was recently discussed in [65] that DRX, which can occur also at cryogenic temperature [67] was not related to the formation of adiabatic shear band and that the latter is a precursor of material failure.

3.3. Microstructure of the deformed HEA samples from X-ray diffraction

The average lattice constants determined for the deformed samples were in the range 0.3403 ± 0.0006 nm. The average crystallite size as well as the dislocations density were determined by XLPA in the sample impacted at the velocity of 10.34 m s^{-1} for a true strain of $\epsilon = 0.49$. As the strain rate increases during dynamic loading, this strain corresponds to a strain rate of 4700 s^{-1} . Fig. 7 shows the corresponding X-ray diffraction pattern in which reflection 222 was omitted due to its weak intensity.

The area-weighted mean crystallite size determined for the sample impacted at the velocity of 10.34 m s^{-1} is 43 ± 6 , which is very close to the crystallite size (39 ± 5 nm) obtained for the sample compressed quasi-statically at the strain rate of $1.5 \times 10^{-3} \text{ s}^{-1}$ [52]. It is noted that in plastically deformed metallic materials the crystallite size obtained by X-ray line profile analysis is usually smaller than the grain size determined by electron microscopy. This difference can be explained by the fact that the crystallite is equivalent to the volume scattering X-rays

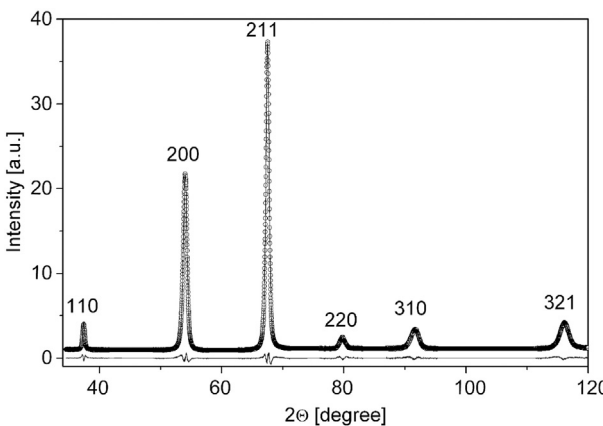


Fig. 7. X-ray diffraction pattern fitting for the sample impacted up to a true strain of ~ 0.49 at the velocity of 10.34 m s^{-1} (corresponds to the strain rate of 4700 s^{-1}). The open circles and the solid line represent the measured data and the fitted curve, respectively. The difference between the measured and the fitted patterns is shown at the bottom. The reflection 222 was omitted due to its weak intensity. It is noted that the values on the vertical axis are not the actual experimental X-ray counts as the CMWP fitting software normalizes the background to one and in this process the overall intensity changes.

coherently and dislocation patterns inside the grains may break the coherency of X-rays. The average dislocation density for the strain rate of 4700 s^{-1} is $47 \pm 7 \times 10^{14} \text{ m}^{-2}$ which is larger than the value determined for quasi-statically compressed specimen ($15 \pm 2 \times 10^{14} \text{ m}^{-2}$ [52]).

At the onset of plastic deformation the flow stress increases monotonously with increasing strain rate as shown in Fig. 1a. In the following the correlation between the dislocation density and the flow stress measured for the sample impacted at the velocity of 10.34 m s^{-1} up to the true strain of $\epsilon = 0.49$ is studied. The flow stress caused by dislocations is usually expressed by the Taylor equation [68]:

$$\sigma = \sigma_0 + \alpha M^T G b \sqrt{\rho}, \quad (1)$$

where σ_0 is the friction stress, α is a constant describing the dislocation hardening, G is the shear modulus, b is the modulus of the Burgers vector (0.2944 nm), M^T is the Taylor factor. The value of M^T in bcc crystals varies between 2.75 and 3.06, depending on the type of slip systems populated by dislocations [69]. If the microstructure is texture-free and the glide occurs only in the most common slip system ($1/2<111>\{110\}$) the Taylor factor is 3.06. In the present study this value was selected for M^T . In a recent study [52] we showed that for the present HEA material $\sigma_0 = 890 \text{ MPa}$, $G = 35 \text{ GPa}$ and $\alpha = 0.16$. Substituting these values and the average dislocation density into eq. (1), 1236 MPa was obtained for the flow stress in the case of the material impacted at the velocity of 10.34 m s^{-1} up to the true strain of $\epsilon = 0.49$. This value is very close to the flow stress obtained by hardness testing (1228 MPa), which suggests that the increment in flow stress at high strain rates is mainly caused by the large dislocation density.

4. Conclusions

The effect of strain rate on the plastic behavior in equimolar $\text{Ti}_{20}\text{Hf}_{20}\text{Zr}_{20}\text{Ta}_{20}\text{Nb}_{20}$ high-entropy alloy was studied in the range of $\sim 10^{-3} \text{ s}^{-1}$ – $3.4 \times 10^3 \text{ s}^{-1}$. The difference in the mechanical performance at various strain rates was explained with the help of post-mortem microstructure investigations using EBSD and XRD. The following results were obtained:

1. The yield strength increased with increasing strain rate. The strength at $3.4 \times 10^3 \text{ s}^{-1}$ was about 40% higher than that measured at the strain rate of $\sim 10^{-3} \text{ s}^{-1}$. The increment in strength becomes faster for the strain rates between $\sim 10^3$ and $\sim 3.4 \times 10^3 \text{ s}^{-1}$.
2. At low and medium strain rates the compression behavior up to the strain of about 0.3 can be characterized by a continuous hardening. At the same time, for high strain rates softening was observed shortly after the onset of plastic deformation. This difference in the mechanical behavior is manifested in the difference between the yield strength and the flow stress measured at the strain of 0.05: at strain rates lower than 10 s^{-1} the yield strength is lower than the flow stress, while for larger strain rates the trend is opposite.
3. EBSD investigations revealed strong strain localization in the samples deformed at high strain rates, which may cause the early softening during compression. It was found that the dispersion of shear bands was reduced with increasing strain rate, i.e. the density and the thickness of bands decreased and increased, respectively.
4. The flow stress measured for the material impacted at the velocity of 10.34 m s^{-1} up to the true strain of ~ 0.49 agrees well with the value calculated from the Taylor equation using the average dislocation density obtained by X-ray line profile analysis. This observation suggests that besides the high friction stress the large dislocation density ($47 \pm 7 \times 10^{14} \text{ m}^{-2}$) is the main reason of the high flow stress of the samples impacted at high strain rates.

Acknowledgments

This work was partly supported by the Hungarian Scientific Research Fund, OTKA, Grant No. K-109021.

References

- [1] B. Cantor, I.T.H. Chang, P. Knight, A.J.B. Vincent, Microstructural development in equiatomic multicomponent alloys, *Mater. Sci. Eng. A* 375–377 (2004) 213–218.
- [2] J.W. Yeh, S.K. Chen, S.J. Lin, J.Y. Gan, T.S. Chin, T.T. Shun, et al., Nanostructured high-entropy alloys with multiple principal elements: novel alloy design concepts and outcomes, *Adv. Eng. Mater.* 6 (2004) 299–303.
- [3] Y. Zhang, T.T. Zuo, Z. Tang, M.C. Gao, K.A. Dahmen, P.K. Liaw, et al., Microstructures and properties of high-entropy alloys, *Prog. Mater. Sci.* 61 (2014) 1–93.
- [4] M.H. Tsai, J.W. Yeh, High-entropy alloys: a critical review, *Mater. Res. Lett.* 2 (2014) 107–123.
- [5] Y.J. Zhou, Y. Zhang, Y.L. Wang, G.L. Chen, Solid solution alloys of AlCoCrFeNiTiX with excellent room-temperature mechanical properties, *Appl. Phys. Lett.* 90 (2007) 181904, <http://dx.doi.org/10.1063/1.2734517>.
- [6] S. Varalakshmi, M. Kamaraj, B.S. Murty, Synthesis and characterization of nanocrystalline AlFeTiCrZnCu high-entropy solid solution by mechanical alloying, *J. Alloys Compd.* 460 (2008) 253–257.
- [7] Y.P. Wang, B.S. Li, M.X. Ren, C. Yang, H.Z. Fu, Microstructure and compressive properties of AlCrFeCoNi high-entropy alloy, *Mat. Sci. Eng. A Struct.* 491 (2008) 154–158.
- [8] S.T. Chen, W.Y. Tang, Y.F. Kuo, S.Y. Chen, C.H. Tasu, T.T. Shun, J.W. Yeh, Microstructure and properties of age-hardenable AlxCrFe1.5MnNi0.5 alloys, *Mater. Sci. Eng. A* 527 (2010) 5818–5825.
- [9] K.B. Zhang, Z.Y. Fu, Effects of annealing treatment on phase composition and microstructure of CoCrFeNiTiAlx high-entropy alloys, *Intermetallics* 22 (2012) 24–32.
- [10] F. Zhang, C. Zhang, S.L. Chen, J. Zhu, W.S. Cao, U.R. Kattner, An understanding of high-entropy alloys from phase diagram calculations, *Calphad* 45 (2014) 1–10.
- [11] Z. Wu, H. Bei, F. Otto, G.M. Pharr, E.P. George, Recovery, recrystallization, grain growth and phase stability of a family of FCC-structured multi-component equiatomic solid solution alloys, *Intermetallics* 46 (2014) 131–140.
- [12] O.N. Senkov, G.B. Wilks, D.B. Miracle, C.P. Chuang, P.K. Liaw, Refractory high-entropy alloys, *Intermetallics* 18 (2010) 1758–1765.
- [13] O.N. Senkov, G.B. Wilks, J.M. Scott, D.B. Miracle, Mechanical properties of Nb25Mo25Ta25W25 and V20Nb20Mo20Ta20W20 refractory high-entropy alloys, *Intermetallics* 19 (2011) 698–706.
- [14] O.N. Senkov, J.M. Scott, S.V. Senkova, D.B. Miracle, C.F. Woodward, Microstructure and room temperature properties of a high-entropy TaNbHfZrTi alloy, *J. Alloys Compd.* 509 (2011) 6043–6048.
- [15] O.N. Senkov, J.M. Scott, S.V. Senkova, F. Meisenkothen, D.B. Miracle, C.F. Woodward, Microstructure and elevated temperature properties of a refractory TaNbHfZrTi alloy, *J. Mater. Sci.* 47 (2012) 4062–4074.
- [16] O.N. Senkov, C.F. Woodward, Microstructure and properties of a refractory NbCrMo0.5Ta0.5TiZr alloy, *Mater. Sci. Eng. A* 529 (2011) 311–320.
- [17] O.N. Senkov, S.V. Senkova, C. Woodward, D.B. Miracle, Low-density, refractory multi-principal element alloys of the Cr–Nb–Ti–V–Zr system: microstructure and phase analysis, *Acta Mater.* 61 (2013) 1545–1557.
- [18] O.N. Senkov, S.V. Senkova, D.B. Miracle, C. Woodward, Mechanical properties of low-density, refractory multi-principal element alloys of the Cr–Nb–Ti–V–Zr system, *Mater. Sci. Eng. A* 565 (2013) 51–62.
- [19] X. Yang, Y. Zhang, P.K. Liaw, Microstructure and compressive properties of NbTiVTaAlx high-entropy alloys, *Proc. Eng.* 36 (2012) 292–298.
- [20] Y. Zhang, X. Yang, P.K. Liaw, Alloy design and properties optimization of high-entropy alloys, *JOM* 64 (2012) 830–838.
- [21] W. Guo, W. Dmowski, J.Y. Noh, P. Rack, P.K. Liaw, T. Egami, Local atomic structure of a high-entropy alloy: an X-ray and neutron scattering study, *Metall. Mater. Trans.* 44 (2013) 1994–1997.
- [22] J.P. Couzinié, G. Dirras, L. Perrière, T. Chauveau, E. Leroy, Y. Champion, I. Guillot, Microstructure of a near-equimolar refractory high-entropy alloy, *Mat. Lett.* 126 (2014) 285–287.
- [23] L. Lilenstein, J.P. Couzinié, L. Perrière, J. Bourgon, N. Emery, I. Guillot, New structure in refractory high-entropy alloys, *Mat. Lett.* 132 (2014) 123–125.
- [24] M. Feuerbacher, M. Heidemann, C. Thomas, Hexagonal high-entropy alloys, *Mat. Res. Lett.* 3 (2015) 1–6.
- [25] Y.P. Wang, D.Y. Li, L. Parent, H. Tian, Improving the wear resistance of white cast iron using a new concept – high-entropy microstructure, *Wear* 271 (2011) 1623–1628.
- [26] Y. Zhang, T.T. Zuo, Y.Q. Cheng, P.K. Liaw, High-entropy alloys with high saturation magnetization, electrical resistivity, and malleability, *Sci Rep* 3 (2013) 1455, <http://dx.doi.org/10.1038/srep01455>.
- [27] A. Gali, E.P. George, Tensile properties of high- and medium-entropy alloys, *Intermetallics* 39 (2013) 74–78.
- [28] C. Zhu, Z.P. Lu, T.G. Nieh, Incipient plasticity and dislocation nucleation of FeCoCrNiMn high-entropy alloy, *Acta Mater.* 61 (2013) 2993–3001.
- [29] F. Otto, A. Dlouly, C. Somsen, H. Bei, G. Eggler, E.P. George, The influences of temperature and microstructure on the tensile properties of a CoCrFeMnNi high-entropy alloy, *Acta Mater.* 61 (2013) 5743–5755.
- [30] Y. Wu, W.H. Liu, X.L. Wang, D. Wang, D. Ma, et al., In situ neutron diffraction study of deformation behavior of a multi-component high-entropy alloy, *App. Phys. Lett.* 104 (2014) 051910.
- [31] W.H. Liu, Y. Wu, J.Y. He, T.G. Nieh, Z.P. Lu, Grain growth and the Hall–Petch relationship in a high-entropy FeCrNiCoMn alloy, *Scripta Mater.* 68 (2013) 526–529.
- [32] L. Patriarca, A. Ojha, H. Sehitoglu, Y.I. Chumlyakov, Slip nucleation in single crystal FeNiCoCrMn high entropy alloy, *Scripta. Mater.* (2015) <http://dx.doi.org/10.1016/j.scriptamat.2015.09.009>.
- [33] Z. Wu, Y.F. Gao, H. Bei, Single crystal plastic behavior of a single-phase, face-center-cubic-structured, equiatomic FeNiCrCo alloy, *Scripta. Mater.* 109 (2015) 108–112.
- [34] N.D. Stepanov, D.G. Shaysultanov, N.Y. Yurchenko, L.A.N. Zherebtsov, et al., High temperature deformation behavior and dynamic recrystallization in CoCrFeNiMn high entropy alloy, *Mater. Sci. Eng. A* 636 (2015) 188–195.
- [35] W. Woo, E.-W. Huang, J.-W. Yeh, H. Choo, C. Lee, et al., In-situ neutron diffraction studies on high-temperature deformation behavior in a CoCrFeMnNi high entropy alloy, *Intermetallics* 62 (2015) 1–6.
- [36] B. Gludovatz, A. Hohenwarter, D. Catoor, E.H. Chang, E.P. George, R.O. Richie, A fracture-resistant high-entropy alloy for cryogenic applications, *Science* 345 (2014) 1153–1158.
- [37] K.-Y. Tsai, M.-H. Tsai, J.-W. Yeh, Sluggish diffusion in Co–Cr–Fe–Mn–Ni high-entropy alloys, *Acta Mater.* 61 (2013) 4887–4897.
- [38] N. Kumar, Q. Ying, R.S. Mishra, Z. Tang, P.K. Liaw, et al., *Mater. Des.* 86 (2015) 598–602.
- [39] M.J. Yao, K.G. Pradeep, C.C. Tasan, D. Raabe, A novel, single phase, non-equiatomic FeMnNiCoCr high-entropy alloy with exceptional phase stability and tensile ductility, *Scripta. Mater.* (72–73) (2014) 5–8.
- [40] Z. Wu, H. Bei, G.M. Pharr, E.P. George, Temperature dependence of the mechanical properties of equiatomic solid solution alloys with face-centered cubic crystal structures, *Acta Mater.* 81 (2014) 428–441.
- [41] H. Couque, The use of the direct impact Hopkinson pressure bar technique to describe thermally activated and viscous properties of metallic materials, *Philos. Trans. A Math. Phys. Eng. Sci.* 372 (2014) 20130218, <http://dx.doi.org/10.1098/rsta.2013.0218>.
- [42] G. Dirras, D. Tingaud, G. Csizár, J. Gubicza, H. Couque, F. Mompou, Characterization of bulk bimodal polycrystalline nickel deformed by direct impact loadings, *Mater. Sci. Eng. A* 601 (2014) 48–57.
- [43] W.S. Lee, C.F. Lin, T.J. Liu, Impact and fracture response of sintered 316L stainless steel subjected to high strain rate loading, *Mater Charact.* 58 (2007) 363–370.
- [44] Q. Xue, X.Z. Liao, Y.T. Zhu, G.T. Gray III, Formation mechanisms of nanostructures in stainless steel during high-strain-rate severe plastic deformation, *Mater. Sci. Eng. A* 410–411 (2005) 252–256.
- [45] J.A. Hines, K.S. Vecchio, Recrystallization kinetics within adiabatic shear bands, *Acta Mater.* 45 (1997) 635–649.
- [46] L.E. Murr, E.A. Trillo, S. Papu, C. Kennedy, Adiabatic shear bands and examples of their role in severe plastic deformation, *J. Mater. Sci.* 37 (2002) 3337–3360.
- [47] W.S. Lee, C.Y. Liu, T.N. Sun, Deformation behavior of Inconel 690 super alloy evaluated by impact test, *J. Mater. Process. Tech.* 153–154 (2004) 219–225.
- [48] Dharan CKH, F.E. Hauser FE, Determination of stress-strain characteristics at very high strain rates, *Exp. Mech.* 1970;10:370–6.
- [49] S. Nafisi, J. Szpunar, H. Vali, R. Ghoshashchi, Grain misorientation in thixo-billets prepared by melt stirring, *Mater Charact.* 60 (2009) 938–945.
- [50] J. Nelson, D. Riley, An experimental investigation of extrapolation methods in the derivation of accurate until-cell dimensions of crystals, *Proc. Phys. Soc. Lond.* 57 (1945) 160–177.
- [51] G. Ribárik, J. Gubicza, T. Ungár, Correlation between strength and microstructure of ball-milled Al–Mg alloys determined by X-ray diffraction, *Mater. Sci. Eng.* 387–389 (2004) 343–347.
- [52] G. Dirras, J. Gubicza, A. Heczel, L. Lilenstein, J.-P. Couzinié, L. Perrière, et al., Microstructural investigation of plastically deformed Ti20Zr20Hf20Nb20Ta20 high-entropy alloy by X-ray diffraction and transmission electron microscopy, *Mater. Charact.* (2015) <http://dx.doi.org/10.1016/j.matchar.2015.08.007>.
- [53] G. Regazzoni, U.F. Kocks, P.S. Follansbee, Dislocation kinetics at high strain rates, *Acta Metall.* 35 (1987) 2865–2875.
- [54] M. Huang, P.E.J. Rivera-Díaz-del-Castillo, O. Bouaziz, S. van der Zwaag, A constitutive model for high strain rate deformation in FCC metals based on irreversible thermodynamics, *Mech. Mater.* 41 (2009) 982–988.
- [55] G. Dirras, H. Couque, J. Gubicza, A. Ouarem, T. Chauveau, P. Jenei, Fine-grained nickel deformed by direct impact at different velocities: microstructure and mechanical properties, *Mater. Sci. Eng. A* 527 (2010) 4128–4135.
- [56] N.N. Guo, L. Wang, L.S. Luo, X.Z. Li, S.U.Y.Q. Li, J.J. Guo, H.Z. Fu, Microstructure and mechanical properties of refractory MnNbHfZrTi high-entropy alloy, *Mater. Des.* 81 (2015) 87–94.
- [57] M.A. Meyers, Y.J. Chen, F. Marquis, D.S. Kim, High-strain, high-strain-rate deformation of tantalum, *Mettal. Mater. Trans.* 26A (1995) 2493–2509.
- [58] O. Man, L. Pantélejev, Z. Pešina, EBSD analysis of phase compositions of trip steel on various strain rates, *Mater. Eng.* 16 (2009) 15–21.
- [59] B. Dodd, Y. Bay, Adiabatic Shear Localization, Second edition, Frontiers and Advances, Elsevier, 2012.
- [60] C. Zener, J.H. Hollomon, Effect of strain rate upon plastic flow of steel, *J. Appl. Phys.* 15 (1944) 22–34.
- [61] B. Barkia, V. Doquet, J.P. Couzinié, I. Guillot, E. Héribert, In situ monitoring of the deformation mechanisms in titanium with different oxygen contents, *Mater. Sci. Eng. A* 636 (2015) 91–102.
- [62] G. Dirras, M. Ota, D. Tingaud, K. Ameyama, T. Sekiguchi, Microstructure evolution during direct impact loading of commercial purity α-titanium with harmonic structure design, *Mater. Tech.* 103 (2015) 311, <http://dx.doi.org/10.1051/matech/2015031>.
- [63] M.A. Meyers, Y.B. Xu, Q. Xue, M.T. Perez-Prado, T.R. McNelley, Microstructural evolution in adiabatic shear localization in stainless steel, *Acta Mater.* 51 (2003) 1307–1325.

- [64] J.F.C. Lins, H.R.Z. Sandim, H.J. Kestenbach, D. Raabe, K.S. Vecchio, A microstructural investigation of adiabatic shear bands in an interstitial free steel, *Mater Sci Eng A* 457 (2007) 205–218.
- [65] D. Rittel, A different viewpoint on adiabatic shear localization, *J. Phys. D Appl. Phys.* 42 (2009) 214009, <http://dx.doi.org/10.1088/0022-3727/42/21/214009>.
- [66] M.T. Pérez-Prado, J.A. Hines, K.S. Vecchio, Microstructural evolution in adiabatic shear bands in Ta and Ta-W alloys, *Acta Mater.* 49 (2001) 2905–2917.
- [67] J.A. Hines, K.S. Vecchio, Recrystallization kinetics within adiabatic shear bands, *Acta Mater.* 45 (1997) 635–649.
- [68] G.I. Taylor, Plastic strain in metals, *J. Inst. Mat.* 62 (1938) 307–324.
- [69] J.M. Rosenberg, H.R. Piehler, Calculation of the Taylor factor and lattice rotations for bcc metals deforming by pencil glide, *Metall. Trans. 2* (1971) 257–259.